



LAWRENCE
LIVERMORE
NATIONAL
LABORATORY

Phase-field modeling of coring during solidification of Au-Ni alloy using quaternions and CALPHAD input

J. L. Fattebert, M. E. Wickett, P. E. A. Turchi

May 7, 2013

Acta Materialia

Disclaimer

This document was prepared as an account of work sponsored by an agency of the United States government. Neither the United States government nor Lawrence Livermore National Security, LLC, nor any of their employees makes any warranty, expressed or implied, or assumes any legal liability or responsibility for the accuracy, completeness, or usefulness of any information, apparatus, product, or process disclosed, or represents that its use would not infringe privately owned rights. Reference herein to any specific commercial product, process, or service by trade name, trademark, manufacturer, or otherwise does not necessarily constitute or imply its endorsement, recommendation, or favoring by the United States government or Lawrence Livermore National Security, LLC. The views and opinions of authors expressed herein do not necessarily state or reflect those of the United States government or Lawrence Livermore National Security, LLC, and shall not be used for advertising or product endorsement purposes.

Phase-field modeling of coring during solidification of Au–Ni alloy using quaternions and CALPHAD input

J.-L. Fattebert^{a,*}, M. E. Wickett^b, P. E. A. Turchi^c

^a Center for Applied Scientific Computing, L-561, Lawrence Livermore National Laboratory, Livermore, CA 94551

^b WCI B Division, Lawrence Livermore National Laboratory, Livermore, CA 94551

^c Physical and Life Sciences, Lawrence Livermore National Laboratory, L-352, Livermore, CA 94551

Abstract

A numerical method for the simulation of microstructure evolution during the solidification of an alloy is presented. The approach is based on a phase-field model including a phase variable, an orientation variable given by a quaternion, the alloy composition, and a uniform temperature field. Energies and diffusion coefficients used in the model rely on thermodynamic and kinetic databases in the framework of the CALPHAD methodology. The numerical approach is based on a finite volume discretization and an implicit time-stepping algorithm. Numerical results for solidification and accompanying coring effect in a Au–Ni alloy are used to illustrate the methodology.

1. Introduction

The microstructure of a material has a large influence on its mechanical properties. An important computational tool to simulate microstructure formation and evolution is the phase-field model (PFM) (for a review, see *e.g.* [1]). In PFM, the basic variable is a phase variable which takes a specific value for each phase present in the simulation. Transition regions between phases are described by a smoothly varying value of that phase variable (diffuse interface) such that the complete field can be easily discretized using an appropriate numerical method. While this approach is used typically for two phases (such as solid and liquid for instance), more phase variables can be added to describe additional phases, or to distinguish grains of different orientations (multi-phase field model). Other fields may include alloy composition, temperature, local elastic deformation, *etc.* PFM is a phenomenological approach, and its parametrization determines bulk energies of each phase as a function of all the variables included in the model, as well as interface energies that may depend in particular on misorientation between two adjacent grains. It is important to provide a realistic parametrization of such models if one expects to gain insights into material properties. This is the reason why various recent research efforts in the field targeting alloy properties have been coupling PFM approaches to a physical database to include known thermodynamic and kinetic properties. To provide a realistic thermodynamic description of all phases in a material, Grafe *et al.* proposed to employ thermodynamic data from databases according to the CALPHAD

method [2] for the multi-component extension to PFM. They used interfaces to the Thermo-Calc and DICTRA software to calculate Gibbs energies, chemical potentials and diffusion matrices. Zhu *et al.* [3] used the CALPHAD method to construct the local free energy in the Cahn–Hilliard equations.

As an alternative to using a very large number of phase-field variables to describe many grains of many different orientations in multi-phase field models, various models representing the local crystallographic orientation and its evolution in time were introduced (orientation-field methods). Our model is closely related to the one introduced by Pusztai *et al.* [4]. Instead of a multi-phase-field model, we use a quaternion to describe the local grain orientation in a crystal. We extend our recent work on this model [5] to include modeling of alloys with composition-dependent diffusion coefficients and free energies parametrized using the CALPHAD methodology. Composition-dependent diffusion coefficients are calculated following the formulation proposed by Andersson and Agren [6]. We use the formulation proposed by Eiken *et al.* [7] for the time-evolution composition equations. Our treatment of binary alloys at interfaces is based on the model proposed by Kim *et al.* [8]. We assume a diffusion controlled time evolution. For simplicity, anisotropy effects are neglected, but crystal symmetries are taken into account. We limit our study to a binary alloy, but the methodology is quite general and can be applied directly to general multi-component alloys.

We apply our methodology to the study of coring in Au–Ni alloys. Using an efficient parallel implementation of an implicit time-stepping algorithm, we are able to study time evolution of grain coarsening over a relatively long time scale. To validate our model and verify our implementation, we compare 1-d results to those from the diffusion

*Corresponding author

Email addresses: fattebert1@llnl.gov (J.-L. Fattebert), wickett1@llnl.gov (M. E. Wickett), turchi1@llnl.gov (P. E. A. Turchi)

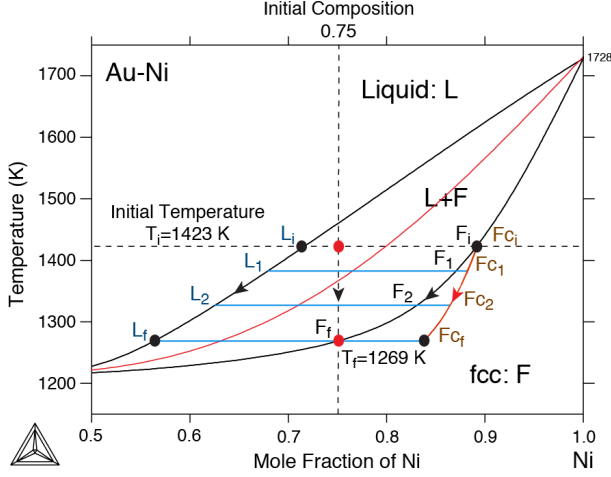


Figure 1: Coring between the liquid state and the fcc phase in Au–Ni alloys. The red line located in the two phase region represents the T_0 curve associated with equal Gibbs energies for the two phases, liquid and fcc.

controlled transformation (DICTRA) software [9, 10].

2. Coring in binary alloys

Since the conditions of “equilibrium” transformation are in practice rarely realized because of the role of kinetics in readjusting phase compositions during a transformation at each temperature increment, a so-called coring phenomenon occurs, characterized by the development of compositional gradient within grains. This is a general phenomenon that has been observed for more than a century in liquid-solid transformations with the prototypical example of freezing in Cu–Ni, and also in solid-solid phase transformations, as soon as the rates of diffusion in the two phases involved in the transformation are different [11]. In a liquid-solid transformation, since the rate of diffusion in the solid phase is always much lower than in the liquid phase, coring cannot be avoided, and homogeneous equilibrium is for practical purposes only maintained in the liquid state. Let us consider a portion of the equilibrium phase diagram for a binary Au–Ni alloy, which is the alloy selected for the present study, characterized by liquidus and solidus lines delineating a two-phase liquid (L) + fcc (F) region as shown in Fig. 1.

In the present example homogeneous equilibrium is maintained in the L phase but not in the F phase since the rate of diffusion is much lower in the solid phase F , *i.e.*, $D_L \gg D_F$. Under equilibrium conditions, let us consider an alloy at the nominal composition AuNi_3 fully equilibrated at $T_1=1423$ K with a proportion of L (L_i) and F (F_i) phases according to the lever rule. The F phase takes from the L phase a disproportionately large amount of the Ni component, causing the L phase to become richer in Au as compared with the nominal alloy composition. As temperature decreases, the trajectories of the composition field for the L and F phases evolve along the (black) lines

indicated by single arrows in Fig. 1. As the temperature is lowered, $T_i > T_1 > T_2$, the L phase becomes richer in Au species and the F phase must also move toward higher Au content. This can only happen by an increase in solid fraction (which contains more Ni than liquid at equilibrium), the preferential adsorption of Au from the L phase and the diffusion of Au species into the F phase formed previously at higher temperature. Because of the strong adjustment in composition in the two phases that needs to occur, departure from equilibrium is to be expected when ordinary cooling rates are used. At the last temperature T_f that indicates the bottom of the two-phase region at the nominal composition AuNi_3 , at about 1269 K, the F phase is richer in Ni than at equilibrium, and because of the slow diffusion within the solid phase, a gradient of composition within each F develops with a higher Ni-content than the equilibrium composition in the center of the grains. Hence a cored structure (*i.e.* exhibiting a gradient of composition) develops inside the F grains with an average composition that evolves along the red line (associated with F_c labels) in Fig. 1, whereas the L matrix is compositionally homogeneous.

Hence, the coring leads to the existence of a Ni-rich (Ni-poor) region in the center (at the edge) of each F grain region that grows in the L matrix as soon as the alloy enters the two-phase region. Because grain growth develops at a different rate than species diffusion, the coring structure is retained in the single-phase field in the region of stability of the F phase. To achieve homogenization, the F phase of Au–Ni has to be annealed at a temperature that does not significantly alter the grain morphology and grain-size distribution (that are both required for engineering applications), and at the same time at a temperature high enough to allow diffusion to take place. Coring has been observed in a large number of alloys during solidification since it occurs as soon as a significant difference in diffusivities of the solute atoms exists between the matrix and the nucleated phases [11], and also in solid phase transformations as in the case of Ga–Pu [12] where the diffusion in the bcc phase is orders of magnitude higher than in the fcc phase resulting in a higher composition of Ga in the center of the fcc grains during transformation.

3. Phase-field model

3.1. Model with local orientation

In our phase-field model, the state of a material is described by state variables that express the phases present in a material, as well as other properties such as composition of various atomic species, temperature, and local grain orientation of a crystal structure at every point in space. We typically consider a finite rectangular domain V to model a representative fragment of a larger macroscopic material with periodic boundary conditions.

We begin by introducing the total free energy functional

$$F_0[\phi, c, \mathbf{q}, T] \equiv \int_V \left\{ \frac{\epsilon_\phi^2}{2} |\nabla \phi|^2 + f(\phi, c, T) + D_{\mathbf{q}}(\phi, T) |\nabla \mathbf{q}| + \frac{\epsilon_{\mathbf{q}}^2}{2} |\nabla \mathbf{q}|^2 \right\} dv, \quad (1)$$

that expresses the total energy of a sample by integrating a local free energy density over the whole sample. Except for the last term, this expression is identical to the model proposed by Pusztai *et al.* [4]. Here ϕ is a structural order parameter indicating matter state (*e.g.*, liquid or solid), c is the composition of a particular species (here we assume a binary material so that $1 - c$ is the composition of the second species), and $\mathbf{q} \equiv (q_1, q_2, q_3, q_4)$ is a quaternion describing local crystallographic orientation, with the normalization

$$\sum_{i=1}^4 q_i^2 = 1. \quad (2)$$

T is the temperature which, in the following, is assumed to be uniform across the computational domain.

The first term in the integrand of the energy functional (1) yields an energy contribution at interfaces between the phases identified by ϕ . The second term represents the bulk energy density at every point in space as a function of the local phase, composition, and temperature. The last two terms yield energy contributions at interfaces between regions of different orientations.

We assume that at every point in space we have the coexistence of a two-phase mixture. We denote these phases L ($\phi=0$) and S ($\phi=1$), by reference to the problem of a mixture of liquid and solid phases, but they can be used to represent other general two-phase problems.

The free energy density, $f(\phi, c, T)$, in the second term of the integrand of (1), is then defined by the phase mixture rule

$$f(\phi, c, T) = (1 - h_\phi(\phi))f^L(c_L, T) + h_\phi(\phi)f^S(c_S, T) + \omega_\phi g_\phi(\phi), \quad (3)$$

where the interpolating polynomial

$$h_\phi(\phi) = \phi^3 (10 - 15\phi + 6\phi^2), \quad (4)$$

introduced to have a smooth transition between phases, satisfies $h_\phi(0)=0$, and $h_\phi(1)=1$. The function g is a “double well” potential of the form

$$g_\phi(\phi) = 16\phi^2(1 - \phi)^2. \quad (5)$$

f^L and f^S are the free energy densities of the L and S phases. They depend on the variables c_L and c_S , that denote the compositions of two locally coexisting phases following the model proposed by Kim *et al.* [8]. They are defined by ϕ and c according to the equations

$$c = [1 - h_\phi(\phi)]c_L + h_\phi(\phi)c_S, \quad (6)$$

$$\tilde{\mu}(x, t) = \frac{\partial f^S}{\partial c_S} \Big|_{c_S=c_S(x, t)} = \frac{\partial f^L}{\partial c_L} \Big|_{c_L=c_L(x, t)}. \quad (7)$$

Equation (7) expresses the condition of equal chemical potentials.

The third term of the integrand of (1) is an orientational free energy where

$$|\nabla \mathbf{q}| = \left(\sum_{i=1}^4 (\nabla q_i)^2 \right)^{1/2} \quad (8)$$

and

$$D_{\mathbf{q}}(\phi, T) \equiv 2HTp(\phi). \quad (9)$$

H is a constant parameter, and p another interpolating monotonic polynomial satisfying $p(0)=0$ and $p(1)=1$. We use $p(\phi) = \phi^2$. The final term in the integrand of (1) involves $|\nabla \mathbf{q}|^2$, and prevents interfaces in \mathbf{q} from becoming too sharp and numerically difficult to represent on a finite mesh. The parameters ϵ_ϕ , ω , H , and $\epsilon_{\mathbf{q}}$ control the interface energy and width.

3.2. CALPHAD methodology

In the CALPHAD approach [13, 14, 15, 16, 17], the Gibbs energy of each individual phase is defined, and the model parameters are collected in a thermodynamic database. It is the modeling of the Gibbs energy of individual phases and the coupling of phase diagram and thermo-chemistry that make the CALPHAD method a powerful technique in computational thermodynamics of multi-component materials. Models for the Gibbs energy are based on the crystal structure of the phases. For pure elements and stoichiometric compounds, the most commonly used model is the one suggested by the Scientific Group Thermodata Europe (SGTE) [18] which has the following form (for simplicity, the pressure dependence and the magnetic contribution are not shown here),

$$G_m - H_m^{SER} = a + bT + cT \ln(T) + \sum_i d_i T^i. \quad (10)$$

The left-hand side of the above equation is defined as the Gibbs energy relative to a standard element reference state (SER), where H_m^{SER} is the enthalpy of the element m in its stable state at 298.15 K and 1 bar of pressure. Coefficients, a , b , c , and d_i are the model parameters. The SGTE data for the most common pure elements of the periodic table have been compiled by Dinsdale [19].

For multi-component solution phases, the Gibbs energy has the following general expression,

$$G = {}^0G + {}^{ideal}G_{mix} + {}^{xs}G_{mix} \quad (11)$$

where 0G is the contribution from the mechanical mixing of the pure components, ${}^{ideal}G_{mix}$ is the ideal mixing contribution, and ${}^{xs}G_{mix}$ is the excess Gibbs energy of mixing due to non-ideal interactions.

In the present case of the binary Au-Ni alloy, a simple single sublattice model is considered for describing the

liquid (L) and solid/fcc (S/F) phases Φ , hence the three contributions to the total Gibbs energy reduce to [13]:

$${}^0G^\Phi = c_{Au} {}^0G_{Au}^\Phi + c_{Ni} {}^0G_{Ni}^\Phi \quad (12)$$

$${}^{ideal}G_{mix} = RT [c_{Au} \ln(c_{Au}) + c_{Ni} \ln(c_{Ni})] \quad (13)$$

$${}^{xs}G_{mix}^\Phi = c_{Au} c_{Ni} \sum_k {}^kL_{Au,Ni}^\Phi (c_{Au} - c_{Ni})^k \quad (14)$$

for $\Phi = L, S$, where the molar Gibbs energy of mixing is expressed by a Redlich-Kister expansion [20]. In these expressions c_i is the composition of the alloy for species i , and the ${}^kL_{Au,Ni}^\Phi$ is the k^{th} -order binary interaction parameter between Au and Ni species expressed as a polynomial in temperature T (usually of first order). Note that the excess Gibbs energy due to non-ideal contributions is expressed within the Muggianu approximation [21]. Data generated with the Thermo-Calc software¹ [22, 23] also provide the basis for more accurate predictions of diffusion kinetics and ultimately TTT (temperature-time-transformations) diagrams with the DICTRA software [9, 22, 23, 24]. Note that the results of both equilibrium solidification and Scheil-Gulliver simulations generated by Thermo-Calc correspond to upper and lower bounds for the DICTRA results.

The thermodynamic data for the liquid state and fcc-based structure of Au-Ni [25] are reported in Appendix D with a complete version of the phase diagram, Fig. D.15, whereas a detailed representation of it is shown in Fig. 1. Note that besides a two-phase (liquid+fcc) region delineated by the liquidus and solidus lines, this system exhibits a fcc miscibility gap below 1089 K.

3.3. PFM coupling

CALPHAD databases provide Gibbs energy densities in J/mol. We assume that molar volumes V_m are independent of composition and define the various PFM free energy densities as the corresponding CALPHAD Gibbs energies divided by V_m . To use the CALPHAD methodology in our phase-field model for a binary alloy, we write the free energy density for the phase Φ – solid (S) or liquid (L) – as

$$f^\Phi(c_\Phi, T) = {}^0f^\Phi(c_\Phi, T) + {}^{ideal}f_{mix}(c_\Phi, T) + {}^{xs}f_{mix}^\Phi(c_\Phi, T) \quad (15)$$

where

$${}^0f^\Phi(c_\Phi, T) = c_\Phi \frac{{}^0G_A^\Phi(T)}{V_m} + (1 - c_\Phi) \frac{{}^0G_B^\Phi(T)}{V_m}, \quad (16)$$

$${}^{ideal}f_{mix}(c_\Phi, T) = \frac{RT}{V_m} [c_\Phi \ln(c_\Phi) + (1 - c_\Phi) \ln(1 - c_\Phi)], \quad (17)$$

and

$$\begin{aligned} {}^{xs}f_{mix}^\Phi(c_\Phi, T) &= c_\Phi(1 - c_\Phi)[{}^0L^\Phi(T) \\ &\quad + {}^1L^\Phi(T)(2c_\Phi - 1) \\ &\quad + {}^2L^\Phi(T)(2c_\Phi - 1)^2]V_m^{-1}. \end{aligned} \quad (18)$$

The coefficients ${}^0L^\Phi$, ${}^1L^\Phi$ and ${}^2L^\Phi$, that depend on temperature, are given for the specific pair of alloy species.

For a phase value ϕ between 0 and 1, we use f as defined in Eq. (3) with f^S and f^L as defined above (Eq. 15). The compositions c_S and c_L are functions of ϕ and c , and Eq. (6)–(7) need to be solved to evaluate expression (15) (see Appendix C).

3.4. Governing equations for phase and orientation variables

To describe the time evolution of the phase and orientation variables, we postulate the Allen-Cahn equations [26]

$$\dot{\phi} = -M_\phi \frac{\delta F}{\delta \phi}, \quad (19)$$

$$\dot{q}_i = -M_{\mathbf{q}} \frac{\delta F}{\delta q_i}, \quad i = 1, \dots, 4, \quad (20)$$

where dots denote temporal derivatives. These equations seek to minimize the energy (Eq. 1) over time subject to the normality constraint on the quaternions (Eq. 2). M_ϕ and $M_{\mathbf{q}}$ are mobility coefficients. We use a constant and uniform mobility for the phase equation. For the orientation mobility on the other hand, we use

$$M_{\mathbf{q}}(\phi) = M_{\mathbf{q}}^{\min} + m(\phi)(M_{\mathbf{q}}^{\max} - M_{\mathbf{q}}^{\min}), \quad (21)$$

where $M_{\mathbf{q}}^{\max}$ varies with the problem and $M_{\mathbf{q}}^{\min} = 10^{-6}$, *i.e.*, very near zero, with $m(\phi)$ an interpolating monotonic polynomial satisfying $m(0) = 1$ and $m(1) = 0$. We use $m(\phi) = 1 - \phi^3(10 - 15\phi + 6\phi^2)$.

We use a Lagrange multiplier to convert the constrained minimization problem to an unconstrained one [4, 5]. The resulting evolution equations for ϕ and \mathbf{q} are then

$$\begin{aligned} \dot{\phi} = M_\phi \left(\epsilon_\phi^2 \nabla^2 \phi - \omega_\phi g'_\phi - 2HTp'(\phi)|\nabla \mathbf{q}| \right. \\ \left. + h'_\phi [f^L(c_L, T) - f^S(c_S, T)] \right. \\ \left. - \tilde{\mu} h'_\phi [c_L - c_S] \right), \end{aligned} \quad (22)$$

$$\begin{aligned} \dot{q}_i = M_{\mathbf{q}}(\phi) \left\{ \nabla \cdot \left(\epsilon_{\mathbf{q}} + \frac{D_{\mathbf{q}}(\phi)}{|\nabla \mathbf{q}|} \right) \nabla q_i \right. \\ \left. - \frac{q_i}{\sum_\ell q_\ell^2} \sum_k q_k \nabla \cdot \left(\epsilon_{\mathbf{q}} + \frac{D_{\mathbf{q}}(\phi)}{|\nabla \mathbf{q}|} \right) \nabla q_k \right\}, \\ i = 1, \dots, 4. \end{aligned} \quad (23)$$

The ordinary differential equations for composition are described in the following subsection.

¹The Thermo-Calc and DICTRA applications software are products of Thermo-Calc AB

3.5. Multi-component diffusion equations

We consider a material made of $n + 1$ species. We denote the mole fraction of each species by $c_i, i = 0, \dots, n$, and by \vec{c} the vector made of the components c_i . If we assume the condition of equal diffusion potential for locally coexisting phases, one can calculate $\vec{c}_S(\vec{c}, \phi)$ and $\vec{c}_L(\vec{c}, \phi)$ by solving a system of non-linear equations (see Eq. 6–7 for two components). We then follow Eiken *et al.* [7], and solve the following diffusion equations

$$\dot{c}_i = \nabla [h_\phi(\phi) D_{ij}^S \nabla c_{S,j} + (1 - h_\phi(\phi)) D_{ij}^L \nabla c_{L,j}], \quad (24)$$

where the usual convention of summation over repeated indexes is being used. To define the matrices of diffusion coefficients in each phase, D^S and D^L , we follow Andersson and Agren [6] under some simpler and less general assumptions (see Appendix B). We suppose in particular that all the components have the same molar volume V_m . According to Eq.(B.18), the diffusion matrix for phase $\Phi = S, L$ is given by

$$D^\Phi = M^\Phi \mathcal{T}^\Phi, \quad (25)$$

where

$$\mathcal{T}^\Phi = \frac{\partial^2 f^\Phi}{\partial c_{\Phi,i} \partial c_{\Phi,j}}, \quad (26)$$

and

$$M_{ki}^\Phi = \sum_{j=0}^n (\delta_{ij} - c_i)(\delta_{jk} - c_k) c_j \Omega_j^\Phi, \quad (27)$$

where Ω_j^Φ is the atomic mobility of component j in phase Φ .

In contrast to (19) and (20), these equations evolve the compositions $c_i, i = 0, \dots, n$, conservatively. These equations are equivalent to [7]

$$\begin{aligned} \dot{c}_i &= \nabla [D_{ij} \nabla c_j \\ &+ D_{ij} (c_{L,j} - c_{S,j}) h'(\phi) \nabla \phi] \end{aligned} \quad (28)$$

with

$$D = h_\phi(\phi) D^S (\mathcal{T}^S)^{-1} \mathcal{T} + (1 - h_\phi(\phi)) D^L (\mathcal{T}^L)^{-1} \mathcal{T} \quad (29)$$

and

$$\mathcal{T}_{ij} = \frac{\partial^2 f}{\partial c_i \partial c_j}, \quad (30)$$

which were proposed in [8] and used in our previous work [5]. The energy function f (Eq. 3) however is not an explicit function of \vec{c} . Thus it is more difficult to compute the derivatives of f with respect to the component of \vec{c} and calculate \mathcal{T} according to Eq. (30) than calculating \mathcal{T}^Φ .

3.6. Atomic mobilities

Since a single-sublattice model is considered for the diffusion of Au and Ni in a Au–Ni matrix, the expression for the activity Gibbs energies of Au and Ni takes a simpler

form. The composition-dependent atomic mobility for a species i in a given phase Φ is given by

$$\Omega_i^\Phi(\vec{c}_\Phi) = \exp(-\Delta G_{i,\Phi}(\vec{c}_\Phi)/RT)/RT \quad (31)$$

where $\Delta G_{i,\Phi}$ is parametrized as a Redlich-Kister expansion

$$\begin{aligned} \Delta G_{i,\Phi} &= \sum_{j=0}^n c_j Q_{i,\Phi}^j \\ &+ \sum_{j=0}^n \sum_{j < k \leq n} c_j c_k \left[\sum_{r=0}^m {}^r Q_{i,\Phi}^{j,k} (c_j - c_k)^r \right] \end{aligned} \quad (32)$$

For example, in a binary alloy made of species A and B , this expansion is often limited to (in a given phase)

$$\begin{aligned} \Delta G_i &= c_A Q_i^A + c_B Q_i^B + c_A c_B {}^0 Q_i^{A,B} \\ &+ c_A c_B (c_A - c_B) {}^1 Q_i^{A,B}. \end{aligned} \quad (33)$$

In this paper, we consider only binary alloys ($n=1$). If we drop the phase index, and consider mobilities, composition, and energies in a given phase, we have for a binary alloy, according to Eq. (B.13),

$$\begin{aligned} M_{00} &= V_m L_{00}'' \\ &= \sum_{j=0}^1 (\delta_{0j} - c_0)(\delta_{j0} - c_0) c_j \Omega_j \\ &= (1 - c_0)(1 - c_0) c_0 \Omega_0 + (-c_0)(-c_0) c_1 \Omega_1 \\ &= (1 - c_0) c_0 [(1 - c_0) \Omega_0 + c_0 \Omega_1] \end{aligned} \quad (34)$$

as in [1], eq.(71).

We verify that in the limit of $c_0 \rightarrow 0$, we obtain

$$\begin{aligned} D &= M_{00} \frac{\partial^2 f}{\partial c^2} \\ &\sim (1 - c_0) c_0 [(1 - c_0) \Omega_0 + c_0 \Omega_1] \frac{RT}{c_0 (1 - c_0)} \\ &\sim \Omega_0 RT \end{aligned} \quad (35)$$

which is relation (B.12).

4. Numerical algorithm

To numerically discretize the system of phase-field equations given by (22), (23), and (24), our approach combines a finite volume spatial discretization with an implicit time integration method. We summarize here the numerical algorithm used to solve the time evolution equations for our phase-field model. More details can be found in a recent publication [5] where a similar methodology is described for a simpler model of alloys (quadratic model for free energies and composition independent diffusion coefficients).

We introduce a uniform grid on the physical domain V and treat the independent variables ϕ , \mathbf{q} , and c as cell-centered quantities with respect to this grid. The finite volume discretization yields a conservative time evolution for the concentration variable.

The spatially discretized model can be written as a system of ordinary differential equations

$$\dot{y}(t) = f(t, y(t)), \quad y(0) = y_0, \quad (36)$$

where

$$y(t) \equiv \begin{pmatrix} \phi(t) \\ \mathbf{q}(t) \\ c(t) \end{pmatrix} \quad (37)$$

and where the components of f are the spatially discretized right-hand sides of (22), (23), and (24) respectively.

The time evolution equations are integrated using variable-order, variable-step backwards difference formulas (BDFs). To preserve the norm of \mathbf{q} during the time integration, it is combined with a coordinate projection. At each discrete time t^n , the use of a BDF results in a non-linear system to be solved for the discrete solution y^n at time t^n

$$G(y^n) = h_n^{-1} \sum_{i=0}^k \sigma_{n,i} y^{n-i} - f(t^n, y^n) = 0, \quad (38)$$

where h_n is the current time step, k is the integration order, and the $\sigma_{n,i}$ are the BDF coefficients.

The non-linear system (38) is solved using a Newton-Krylov algorithm where the Jacobian is computed by finite differences. The Jacobian system is solved using a Generalized Minimum Residual (GMRES) iteration scheme [27] with a diagonal block preconditioner. As preconditioner, we employ a multigrid preconditioned conjugate-gradient solver from the *Hypre* library [28] for each diagonal block.

For the diagonal block corresponding to the time evolution equation for c , we use a preconditioner for the GMRES solver based on Eq. (28) as in [5]. This equation is equivalent to Eq. (24) before discretization, and is more appropriate than (24) since it explicitly involves ∇c on the right hand side. However, we replace D , Eq. (29), with the simpler approximation

$$\tilde{D} = h(\phi) D^S + [1 - h(\phi)] D^L. \quad (39)$$

In our phase-field code AMPE, we employ the general-purpose integrator CPODES [29] to integrate the system (36). CPODES solves systems of ordinary differential equations with invariants using the combination of BDF, coordinate projection, and Newton-Krylov type algorithms summarized above. CPODES is a time integrator with coordinate-projection capability based on the CVODES integrator, which is part of the *Sundials* package [30].

Crystal symmetries are taken into account when evolving quaternion orientations and computing quaternion differences. This is done using the algorithm described in Appendix A.

To calculate the compositions in each phase at each step of the algorithm, the system of non-linear equations (6–7) is solved using a damped Newton solver (see Appendix C). Some authors avoid solving these equations exactly

at every step, considering it time consuming [31]. In an implicit time-stepping algorithm, since fewer evaluations of the right hand-side are required, this is not so expensive and is done at every step. Also, unlike the methodology proposed by Grafe *et al.* [2], for instance, our solver is directly implemented in our code, and no coupling to an external software such as DICTRA is necessary.

5. Numerical results

We use the model described above and its implementation to simulate coring during solidification in a Au–Ni alloy. In this section, we choose to plot the composition c_1 , the mole fraction of Ni in the alloy, and c refers to that composition.

5.1. Phase-field model and numerical parameters

Equilibrium bulk energies and diffusion coefficients are based on current knowledge of the physical properties of the Au–Ni alloy and its phase diagram. For the face-centered cubic (fcc) phase, we use diffusional mobilities as assessed by Wang *et al.* [32]. For the liquid phase, we refer to Ref. [33] to calculate the mobility parameters for the Au–Ni system according to:

$$Q_I^J = \alpha_J + RT \ln(\beta_I^J) \quad (40)$$

with

$$\alpha_J = -R (0.17 T_J^{Melt} [16 + K]) \quad (41)$$

$$\beta_I^J = (8.95 - 0.0734 Z_J) \cdot 10^{-8} \frac{d_J}{d_I} \quad (42)$$

where Z_J is the atomic number for species J (28 and 79 for Ni and Au, respectively), d_J is the Goldsmith diameter (0.2884 and 0.2492 nm for Au and Ni respectively), T_J^{Melt} is the melting temperature (1338 and 1726 K for Au and Ni, respectively), and $K=3$ by reference to the solid phase (here fcc). Model coefficients for mobilities are given in Appendix E.

For the description of the alloy energetics, we use CALPHAD thermodynamic data (see Appendix D). Fig. 2 illustrates the energy landscape for the independent variables ϕ and c at $T=1450$ K. The equilibrium compositions for this temperature are $c_L^{eq}=0.742$ for the liquid phase and $c_S^{eq}=0.904$ for the solid (fcc) phase. We assume a molar volume independent of phase and composition. We use $V_m = 4.8 \cdot 10^{-5} \text{ m}^3/\text{mol}$.

There remains a few parameters to setup to fully characterize our model. First, the mobilities M_ϕ and M_q^{\max} are determined by assuming a diffusion-controlled process, and by simulating a solid single grain growth (positive growth with decreasing temperature) embedded in a liquid matrix. These mobilities should be large enough to reach a diffusion-controlled regime (time evolution independent of mobilities), but not too large to avoid slowing down the numerical scheme used for time integration. Note that

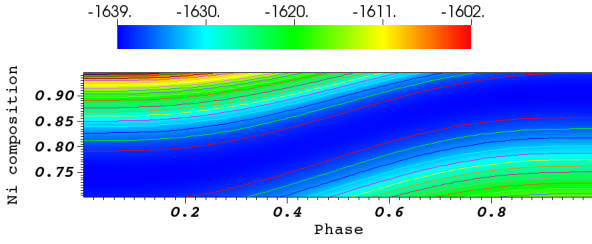


Figure 2: Bulk free energy as a function of phase (0=L, 1=S) and Ni at.% composition at $T=1450$ K (initial temperature for 2-d simulations of section 5.4). Units: $\text{pJ}/\mu\text{m}^3$.

for initial conditions given by non-equilibrated grains with sharp interfaces, the initial steps will still depend on the choice of these mobilities. Thus it is important to start from an equilibrated grain at the initial temperature to carry out this simulation. The values obtained for M_ϕ and M_q^{\max} are listed in Table 1.

The remaining parameters (ϵ_ϕ , ϵ_q , ω and H) are linked to solid-solid and solid-liquid interface energies and width. These four parameters determine all the interface energies for all the possible interfaces between two solid grains of various orientations. Therefore there are not enough tuning parameters to reproduce exactly all the interface energies between various pairs of grains if those were known. Since we are not aware of any interface energy data for Au-Ni, we limit our tuning to simply determine values leading to realistic energies. The main challenge is to find parameters that lead to “wet” interfaces — for which ϕ goes to zero in the middle of the interface — for typical grain misorientations, with proper numerical properties (reasonable interface width) and reasonable energies. The parameters we use are listed in Table 1.

ϵ_ϕ	0.2	$(\text{pJ}/\mu\text{m})^{1/2}$
ϵ_q	0.25	$(\text{pJ}/\mu\text{m})^{1/2}$
ω	0.4	$\text{pJ}\mu\text{m}^{-3}$
M_ϕ	10.0	$\text{s}^{-1}\text{pJ}^{-1}$
M_q^{\max}	1.0	$\text{s}^{-1}\text{pJ}^{-1}$
H	0.08	$\text{pJK}^{-1}\mu\text{m}^{-1}$

Table 1: Parameters for Au-Ni PFM simulations.

For spatial numerical discretization, we use a mesh spacing $h=0.0125 \mu\text{m}$ for the 2-d and 3-d numerical simulations presented in this paper. The bi-layers simulation in Section 5.3 will justify that choice.

5.2. Verification

To verify our implementation of the model described above, we run 1-d calculations to be compared with sharp-interface results from the DICTRA software [9, 22, 23, 24]. A similar benchmark was used by other authors [2, 34] to verify their multi-phase-field model. We run a solidification simulation, starting from a small solid (fcc) grain

within a liquid environment at 1423 K at a nominal alloy composition of 75 at.% Ni. Before lowering the temperature, the time-evolution equations are integrated at a fixed temperature until both the solid grain and the liquid environment reach their respective equilibrium compositions at this temperature (*i.e.*, $c_{Ni}^L=0.7169$ and $c_{Ni}^S=0.8918$), and the origin of time is set up once equilibration is achieved. In the PFM approach, the smoothly varying phase variable at the solid-liquid interface leads to a diffused interface, the width of which is controlled by ϵ_ϕ . Then the temperature is uniformly lowered across the system at a constant cooling rate of -5 K/s. The total sample size is chosen to be $3.2 \mu\text{m}$. In Fig. 3, we show the Ni composition profile along the 1-d structure for various times up to 28 s (*i.e.*, down to a temperature of 1283 K). To start the DICTRA calculations, it is assumed that the thicknesses of the fcc and liquid regions are in accordance with the equilibrium data at 1423 K, *i.e.*, 0.606137 and $2.593863 \mu\text{m}$ for the solid (fcc) and liquid regions, respectively.

As clearly shown in Fig. 3 there is excellent agreement between the DICTRA and 1-d PFM results, except for the minor differences associated with the diffuse and sharp interface in the case of PFM and DICTRA, respectively. Hence the results on position of the solid-liquid interface and interface velocity as functions of time are expected to be almost the same in both approaches. Note that for PFM to approximate well a sharp interface, we used $\epsilon_\phi = 0.1$ and $\omega = 1.6$ for this verification test. With the parameters of Table 1, the interface width would be four times wider and its velocity about 4% larger.

An enhancement of the Ni composition in the solid region away from the solid-liquid interface is observed when compared to equilibrium results (see Fig. 3), and this coring phenomenon increases with time, *i.e.*, with a decrease in temperature, as expected. Other DICTRA calculations were performed at various cooling rates, and Fig. 4 shows the interface position and its velocity as functions of temperature for $dT/dt=-1, -5, -25, -50, -100$ K/s. As expected the velocity increases whereas the fcc grain size decreases with the cooling rate. Note that for the selected nominal alloy composition, the location of the solidus line is at about 1269 K (see Fig. 1). For this set of data we define a quantitative measure of coring in a grain by the following coring factor

$$\delta c = \left[\frac{1}{V_{\text{grain}}} \int_{\text{grain}} |c - \bar{c}|^2 dv \right]^{1/2} \quad (43)$$

where \bar{c} denote the average value of c in the grain, and V_{grain} is the grain volume. A grain is identified as a connected region of the computational domain for which $\phi > 0.85$. Note that a different expression was proposed by Hu *et al.* [35] to quantify coring in a sample that takes an average over the whole sample, and does not take into account individual grains.

The bottom of Fig. 4 shows this coring as a function of temperature for various quenching rates. As expected the

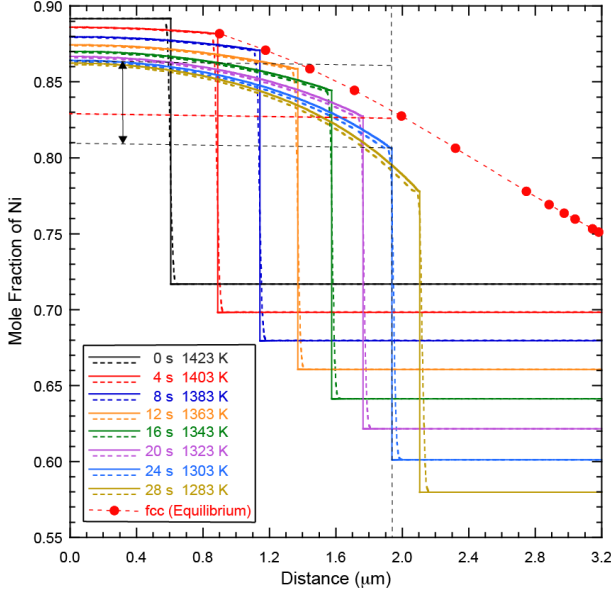


Figure 3: Comparison between DICTRA (solid lines) and 1-d PFM (dashed lines) results on coring in AuNi₃ starting from 1423 K (in the two-phase region, liquid+fcc, see Fig. 1) and with a cooling rate $dT/dt = -5$ K/s. Also indicated in the figure is the mole fraction of Ni versus distance assuming thermodynamic equilibrium (red dashed line and circles). As an example at 1303 K (*i.e.*, corresponding to a time of 24 s), the black double-arrow solid line indicates the gradient of Ni composition (*i.e.*, the amount of coring) compared to the equilibrium composition indicated by the red dashed line.

coring increases with the quenching rate although clearly the increase in coring is limited by the thermodynamic driving force as the quenching rate increases.

5.3. Bi-layer simulations

In general, the interface energy depends not only on the misorientation between two adjacent grains, but also on the normal to the interface. In our model, the interface energy is determined by only four parameters, ϵ , ω , H , and ϵ_q , and does not depend on the normal to the interface. Within these constraints, a sensible option is to tune those parameters to obtain reasonable values for the interface energy over the range of possible misorientations. This is typically sufficient considering the experimental values for those energies are often difficult to obtain.

To study and fully characterize interfaces in our model, we run simulations for a 1-d system made of two solid grains with different crystal orientations and periodic boundary conditions (see Fig. 5). We select a nominal composition of 75 at. % Ni/25 at. % Au and a temperature of 1250 K (in the solid region of the phase diagram). We run the simulations until equilibrium is reached throughout the system for various misorientation angles between the two adjacent grains. No rotation of grains occurs since M_q is set to zero in the solid phase, but the solid grains fill up space except for the diffuse interface between the two grains. In Fig. 6, we plot the equilibrium values of the variables in our model, ϕ , c , and the first two components

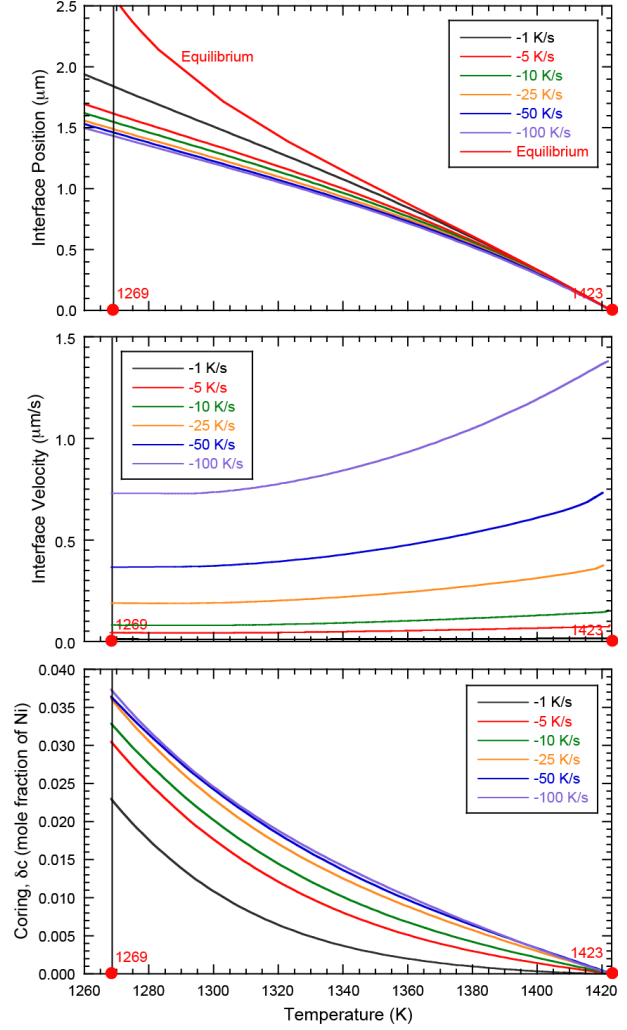


Figure 4: Interface position (top) and velocity (middle), and coring δc versus temperature (or time) for various cooling rates (-1, -5, -10, -25, -50, and -100 K/s) according to DICTRA calculations in the case of AuNi₃ during quenching in the two-phase fcc+liquid region (between the starting temperature of 1423 K and the final temperature of 1269 K). In the top figure, the initial position of the fcc-liquid interface at 1423 K is taken as zero of position, and the interface position according to equilibrium composition (red solid line) is also reported for comparison.

of \mathbf{q} , as functions of the position with respect to one of the interfaces, $x = 0$ denoting the middle of the interface, for a small and a large misorientation. In both cases, the middle of the interface is fully liquid and c tends towards the liquid equilibrium composition in that region. As expected, the width of the interface becomes wider for larger misorientation.

In Fig. 7, we plot the various components making up the interface energy as functions of the angle between the two grains, as well as the system total grand potential (GP)

$$\Omega[\phi, \mu, \mathbf{q}, T] = F[\phi, c, \mathbf{q}, T] - \int_V \mu c dv \quad (44)$$

where $\mu = \partial f / \partial c$. The total GP is the appropriate value to compare energies between various systems (various mis-

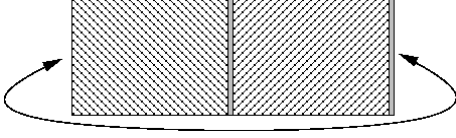


Figure 5: Two adjacent solid grains of different orientations in a 1-d arrangement with periodic boundary conditions.

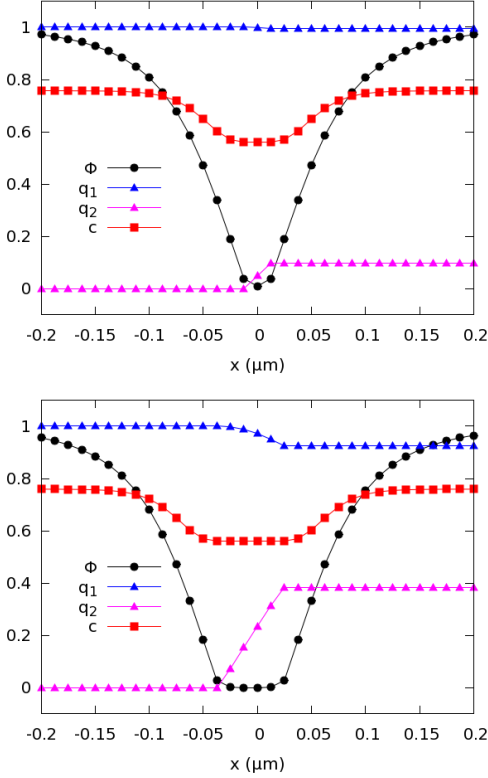
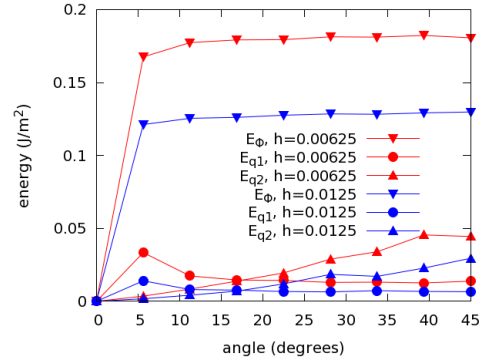


Figure 6: Profile of relevant variables (ϕ, q_1, q_2, c) through bi-layer interface after reaching equilibrium at $T=1250$ K, in the case of a small misorientation (11.25 deg., top) and a large misorientation (45.0 deg. bottom).

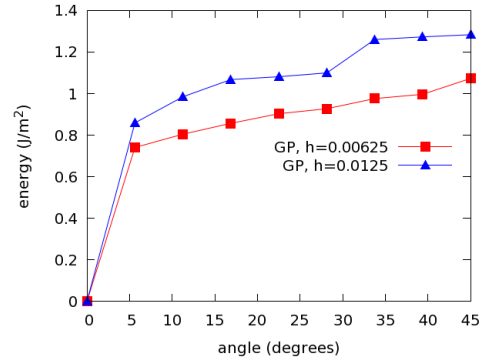
orientations) in this context (see [36]). As expected, its value monotonically increases with the misorientation angle. The energy is plotted for a mesh spacing $h=0.0125$ μm , the one used for 2-d and 3-d simulations, and for a finer mesh spacing $h=0.00625$ μm . This shows that while a mesh spacing of $h=0.0125$ μm leads to results slightly different than those obtained with a finer mesh spacing, the energies are already sufficiently accurate for our purpose.

5.4. 2-d Microstructure formation during cooling process

We carry out a series of 2-d simulations of solidification in AuNi_3 , and follow the microstructure formation during the cooling process. The simulations begin in the two-phase region at $T=1450$ K and $c=0.75$. For all the simulations, the initial state is defined by a certain number (144) of solid seeds at their equilibrium composition ($c = c_S^{eq}$) embedded in a liquid matrix also at equilibrium composition ($c = c_L^{eq}$) (see Figs. 8 and 11). Our simula-



(a) Various terms composing the interface energy. E_ϕ refers to the second-order term in $\nabla\phi$ in the energy functional, see Eq. (1), while E_{q1} and E_{q2} refer to the first- and second-order terms in \mathbf{q} respectively.



(b) Total Grand-potential (GP), Eq. (44)

Figure 7: Interface energy terms and GP as functions of misorientation for resolution used in numerical applications ($h=0.0125$ μm) and for a resolution twice as fine ($h=0.00625$ μm), at a fixed temperature ($T=1250$ K).

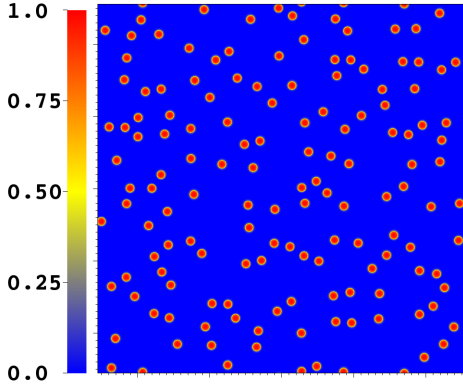


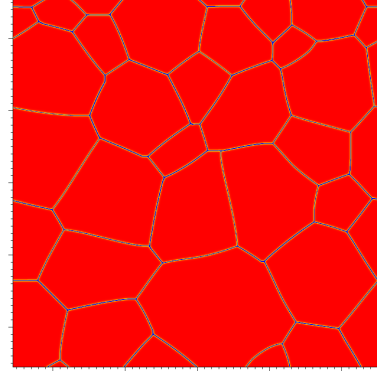
Figure 8: Initial conditions and color scheme for phase value ϕ in 2-d solidification simulations: solid grains (red) embedded in the liquid matrix (blue). The size of the domain is $25.6 \mu\text{m} \times 25.6 \mu\text{m}$.

tions are performed in a square domain $25.6 \mu\text{m} \times 25.6 \mu\text{m}$ with periodic boundary conditions. The position of the seeds are defined by adding a random displacement to a 12×12 uniform distribution. The quaternion associated with each seed is randomly selected on the 4-d hypersphere of unit quaternions. The computational domain is numerically discretized with a uniform mesh 2048×2048 . The initial number of seeds is chosen small enough so that their sizes are large enough to be stable during the initial time steps, in particular when interfaces evolve from the initial sharp interfaces into smoother interfaces numerically well described on the mesh.

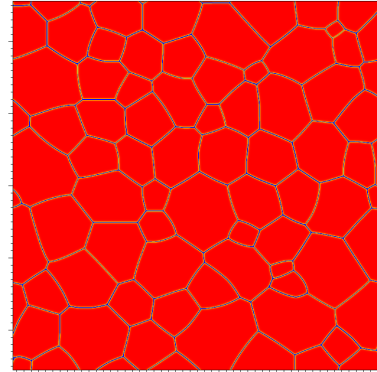
We investigate the effect of the cooling rate on the resulting microstructures once a fully solid phase is reached at $T=1150 \text{ K}$. Fig. 9 shows the microstructures obtained for $dT/dt=-10 \text{ K/s}$, $dT/dt=-25 \text{ K/s}$, and $dT/dt=-100 \text{ K/s}$. Figure 9 also shows the orientation field (quaternion) for the microstructure obtained with $dT/dt=-100 \text{ K/s}$, where the four components of the quaternions have been mapped into a RGB color map. For a fast cooling rate $dT/dt=-100 \text{ K/s}$, the final number of grains (142) is almost identical to the initial number of grains. For a cooling rate 10 times slower, $dT/dt=-10 \text{ K/s}$, the final number of grains (26) is much smaller. Fig. 10 shows the evolution of grain sizes with time for these two cases. The difference is due to Oswald ripening: various grains grow for a very short time and then disappear early on in the process. For faster cooling rates, grains grow faster, and many more grains can grow fast enough to overcome Oswald ripening. Figure 12 shows composition inhomogeneities (coring) in the microstructures formed during the cooling process.

In Fig. 13, we plot the coring factor δc (Eq. 43) as a function of time for each grain for the simulations with $dT/dt=-10 \text{ K/s}$ and $dT/dt=-100 \text{ K/s}$. The slower cooling rate leads to a larger coring factor as larger grains with composition gradients are formed.

A determinant factor in these simulations is the ratio



(a) $dT/dt=-10 \text{ K/s}$ after 30 s.



(b) $dT/dt=-25 \text{ K/s}$ after 12 s.



(c) $dT/dt=-100 \text{ K/s}$ after 3 s.

Figure 9: Phase ϕ value in microstructures obtained when reaching $T=1150 \text{ K}$ for various cooling rates ($\phi=0$ for liquid, blue, $\phi=1$ for solid, red). For the fastest cooling rate ($dT/dt=-100 \text{ K/s}$), we show the quaternion field instead of ϕ (c).

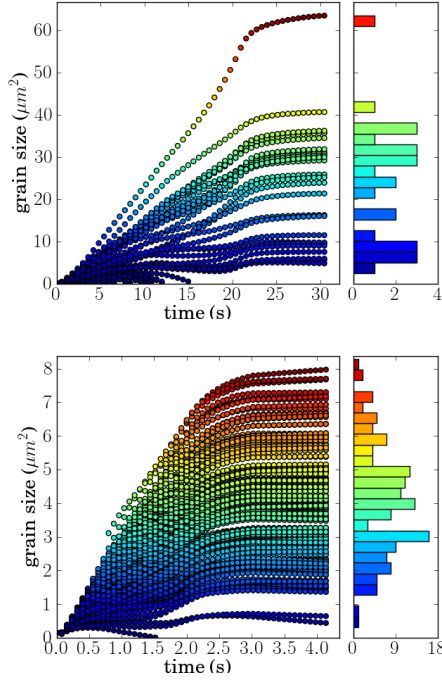


Figure 10: Size of each solid grain as a function of time for $dT/dt = -10$ K/s (top) and $dT/dt = -100$ K/s (bottom). The distribution of grains according to their sizes at the end of the simulation is shown on the right of each plot. Note the different scales used for the y-axis.

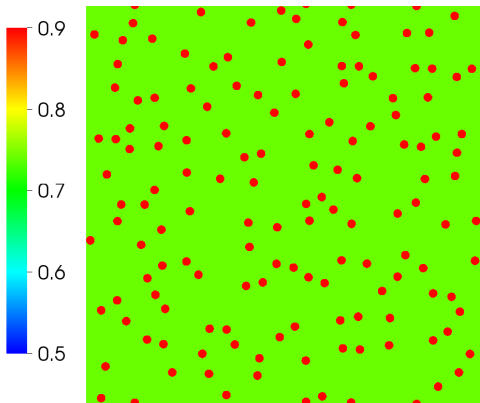
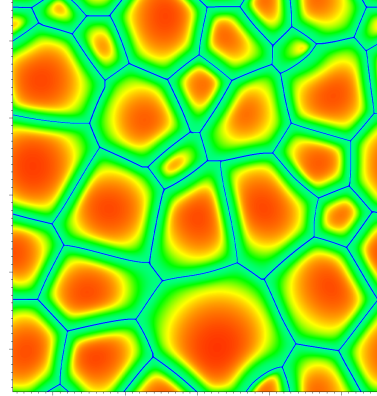
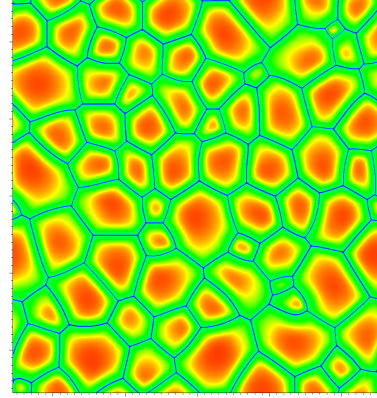


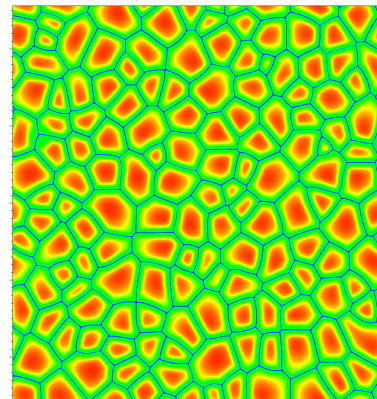
Figure 11: Initial composition field and color scheme for 2-d cooling simulations (same simulations as in Fig.9). The size of the domain is $25.6 \mu\text{m} \times 25.6 \mu\text{m}$.



(a) $dT/dt = -10$ K/s after 30 s.



(b) $dT/dt = -25$ K/s after 12 s.



(c) $dT/dt = -100$ K/s after 3 s.

Figure 12: Composition field obtained when reaching $T = 1150$ K for various cooling rates (a)-(c) (same simulations as in Fig. 9). The size of the domain is $25.6 \mu\text{m} \times 25.6 \mu\text{m}$.

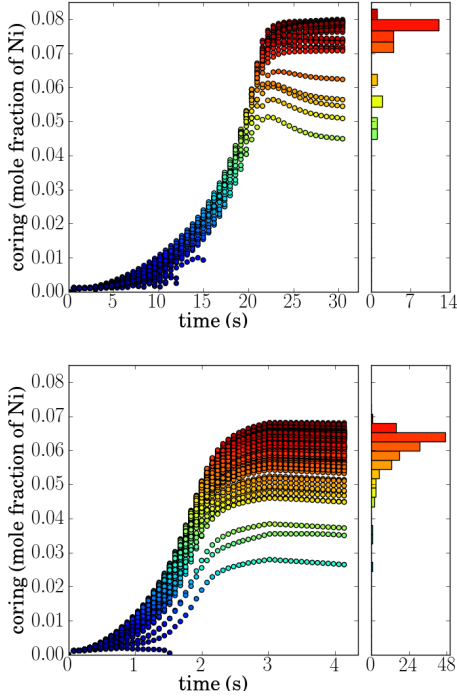


Figure 13: Coring (δc), given by Eq. (43), vs. time for $dT/dt = -10$ K/s (top) and $dT/dt = -100$ K/s (bottom). The distribution of grains according to coring at the end of the simulation is shown on the right of each plot.

between the cooling rate and the diffusion rate in the solid phase. A simulation with $dT/dt = -100$ K/s would lead to the same results as those obtained with $dT/dt = -10$ K/s if the diffusion coefficient in the solid phase was 10 times larger and the mobilities were also 10 times larger (factor 10 in each time evolution equation). From that point of view, slow diffusion in the solid phase is responsible for the formation of larger grains and more coring.

5.5. 3-d Microstructure formation during cooling process

To illustrate the capability we have developed, we also carry out 3-d simulations performed in a cubic domain $3.2 \mu\text{m} \times 3.2 \mu\text{m} \times 3.2 \mu\text{m}$, with periodic boundary conditions. The domain is discretized with a uniform mesh $256 \times 256 \times 256$, and the initial conditions are set up at $T = 1450$ K with 27 solid grains at equilibrium composition. While 3-d calculations are much more computer intensive, we can still study solidification in AuNi_3 over periods of time of the order of seconds with an efficiently parallelized code. A simulation of 3 seconds of time evolution with a cooling rate $dT/dt = -100$ K/s requires 19,300 steps. This takes about 48 hours wall-clock time on 512 processors (32 nodes of Intel Xeon E5-2670 InfiniBand cluster). Figure 14 shows the composition and the quaternion fields obtained after decreasing the temperature for 3 s. One can observe that in 3-d, initial small grains are even less stable than in 2-d and need to be quite large to survive Oswald ripening during the initial steps.

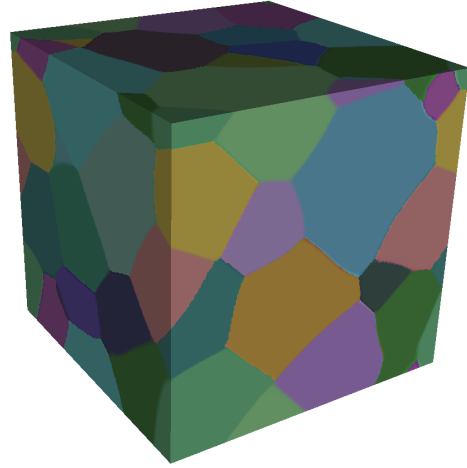
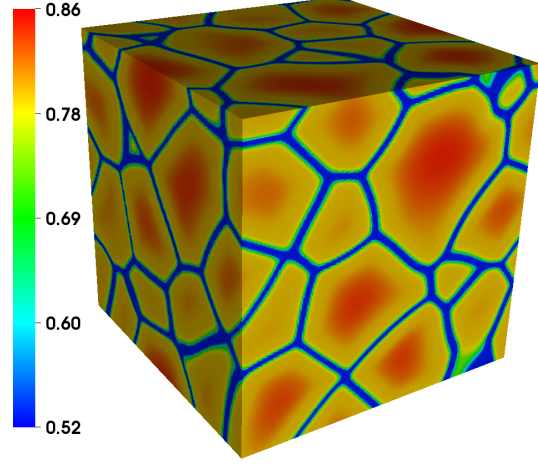


Figure 14: 3-d simulations: composition (top) and quaternion/orientation (bottom) fields obtained when reaching $T = 1150$ K for $dT/dt = -100$ K/s. The domain size is $3.2 \mu\text{m} \times 3.2 \mu\text{m} \times 3.2 \mu\text{m}$.

6. Conclusion

In this paper, we presented an application of phase-field modeling to the study of alloys solidification in real materials. Our numerical scheme is based on a finite volume discretization of the phase-field equations, including a phase variable, the alloy composition, and a 4-components quaternion variable to describe grain orientations. An adaptive implicit time-stepping algorithm is used to accurately evolve these fields in time. An algorithm is proposed to take into account crystal symmetry when comparing grain orientations defined by quaternions. This numerical approach combined with PFM parameters obtained from realistic data given by the CALPHAD methodology appears to be an effective approach to study solidification and grain structure formation in alloys. The approach scales well with the number of grains, thanks to the use of quaternions that does not require an increase in the number of variables with problem size. It also parallelizes well and allows fast simulations on large parallel supercomputers.

We applied our methodology to the particular case of a binary alloy, Au–Ni, for which we provide a complete set of parameters. Simulations in 1-d, 2-d and 3-d are presented. 1-d PFM results are in excellent agreement with DICTRA calculations. A detailed analysis of the behavior of the various variables at grain interfaces is also provided. Simulations of solidification are carried out by reducing the value of a uniform temperature field for initial conditions with random solid seeds. Numerical evidence of coring in this system is obtained for various cooling rates, and the major influence of the cooling rate and coring on the final microstructures is demonstrated.

Acknowledgments

The authors are grateful to Nele Moelans, Ming Tang and Milo Dorr for useful discussions. P.T. would also like to thank Lars Höglund for useful insights. This work was performed under the auspices of the U.S. Department of Energy by Lawrence Livermore National Laboratory under Contract DE-AC52-07NA27344. Work at LLNL was funded by the Laboratory Directed Research and Development Program under project tracking code 12-SI-008.

Appendix A. Quaternion differences and crystal symmetry

The mapping from unit quaternions to rotations is 2-to-1: two quaternions on opposite sides of the 4-d hypersphere are equivalent. Additionally, crystal structure symmetries imply that several other quaternions are equivalent. Cubic crystals (*i.e.*, fcc) have 24 symmetrically related orientations that are physically indistinguishable. Therefore, taking into account the 2-to-1 ambiguity, there are 48 equivalent quaternions on the 4-d hypersphere.

When comparing two quaternions in calculating finite differences in our numerical scheme, we need to find the minimum difference that accounts for these equivalent quaternions. In practice, instead of searching all 48 possible equivalent quaternions, we keep track of the rotations one needs to apply to each cell to obtain an equivalent quaternion closest to the one in the adjacent discretization cell (quaternion values are defined at cell centers). In general, these rotations do not vary in time, as quaternions vary smoothly in space, differing by small amounts between neighboring cells, which persist during time evolution. Thus these rotations need to be computed only once at the beginning and stored for the duration of the simulation.

During a simulation it is still possible to find two neighboring grains having quaternion orientations differing by more than the maximal difference allowed by symmetry. This is possible because the diffuse interface involves several grid points, and the difference between quaternion orientations of two grains is made of the sum of the differences over the grid points in the diffuse interface region. This can come about for instance, when a grain C is squeezed between two other grains A and B , and disappears. This leaves a quaternion difference between A and B larger than allowed by symmetry, while the differences between C and A or C and B were smaller than the maximum allowed by symmetry.

We handle this situation with the following algorithm. At regular time intervals, we count the number of grains. A grain is defined by a compact domain where ϕ is above a certain threshold value (solid). If the number of grains counted is smaller than in the previous count, we extend the value of the quaternions in solid grains into the liquid regions by setting \mathbf{q} in liquid cells to the value of the closest solid grain, as if all the grid points were in the solid phase. This produces sharp interfaces in orientation, allowing us to recalculate the rotations at each cell interface based on the new values of the quaternions. This ensures that the symmetry rotation between two adjacent grains is properly computed. Then we relax the quaternion field by evolving Eq. (23), while all the other variables are kept frozen. Since accuracy in time integration for this relaxation process is not important, this process of relaxation can be sped up by first applying a local cell averaging scheme several times in the liquid region to smooth out the quaternion discontinuities. Tolerance on time integration can also be relaxed. Once this relaxation process is terminated, the regular time evolution is restarted. This process can be considered as an alternative to the algorithm proposed in [37] for simple angles in 2-d.

Appendix B. Multi-component diffusion

Following Andersson and Agren [6] under some simpler and less general assumptions, we consider an alloy made of $n + 1$ species. We suppose all the components have the same molar volume V_m , and denote the mole fraction of

each species by $c_k, k = 0, \dots, n$. The mole fractions (or compositions) satisfy

$$\sum_{i=0}^n c_k = 1. \quad (\text{B.1})$$

Compositions evolve in time according to diffusion equations of the form

$$\frac{\partial c_k}{\partial t} = -V_m \nabla \cdot \mathbf{J}_k \quad (\text{B.2})$$

where \mathbf{J}_k are fluxes. In the linear theory, we express the fluxes as linear functions of the driving forces. If the driving forces are chemical potentials, we have

$$\mathbf{J}_k = -\sum_{j=0}^n L_{kj} \nabla \mu_j \quad (\text{B.3})$$

where the L_{kj} are phenomenological parameters that relate fluxes to driving forces, and

$$\mu_i = \frac{\partial g}{\partial c_i} \quad (\text{B.4})$$

is the chemical potential of component i associated with the free energy

$$g(c_0, c_1, \dots, c_n). \quad (\text{B.5})$$

The fluxes must satisfy

$$\sum_{k=0}^n \mathbf{J}_k = 0 \quad (\text{B.6})$$

independently of the frame of reference (which could be moving with a velocity v). By eliminating c_n using (B.1) and enforcing (B.6) independently of the frame of reference, Andersson and Agren [6] obtain

$$\mathbf{J}_k = -V_m^{-1} \sum_{j=0}^{n-1} D_{kj}^n \nabla c_j \quad (\text{B.7})$$

where

$$D_{kj}^n = D_{kj} - D_{kn}, \quad (\text{B.8})$$

$$D_{kj} = V_m \sum_{i=0}^n L_{ki}'' \frac{\partial [\mu_i - \mu_n]}{\partial c_j}, \quad (\text{B.9})$$

$$L_{ki}'' = \sum_{j=0}^n \sum_{r=0}^n (\delta_{ir} - c_i)(\delta_{jk} - c_k) L_{jr}, \quad (\text{B.10})$$

and L is a diagonal matrix

$$L_{kj} = c_k \Omega_k \delta_{kj} V_m^{-1}. \quad (\text{B.11})$$

The scalar parameter Ω_k is a mobility directly related to the tracer diffusivity D_k^* through Einstein's relation

$$D_k^* = RT \Omega_k. \quad (\text{B.12})$$

Equation (B.10) can be written more simply as

$$L_{ki}'' = \sum_{j=0}^n (\delta_{ij} - c_i)(\delta_{jk} - c_k) c_j \Omega_j V_m^{-1}. \quad (\text{B.13})$$

Now if we eliminate c_n using (B.1), we can write

$$f(c_0, c_1, \dots, c_{n-1}) = g \left(c_0, c_1, \dots, c_{n-1}, 1 - \sum_{i=0}^{n-1} c_i \right) \quad (\text{B.14})$$

We then have

$$\tilde{\mu}_i = \frac{\partial f}{\partial c_i} = \frac{\partial g}{\partial c_i} - \frac{\partial g}{\partial c_n} = \mu_i - \mu_n \quad (\text{B.15})$$

and

$$\begin{aligned} \frac{\partial^2 f}{\partial c_i \partial c_j} &= \frac{1}{\partial c_j} \left(\frac{\partial g}{\partial c_i} - \frac{\partial g}{\partial c_n} \right) - \frac{1}{\partial c_n} \left(\frac{\partial g}{\partial c_i} - \frac{\partial g}{\partial c_n} \right) \\ &= \frac{1}{\partial c_j} (\mu_i - \mu_n) - \frac{1}{\partial c_n} (\mu_i - \mu_n). \end{aligned} \quad (\text{B.16})$$

Thus Eq.(B.8) becomes

$$D_{kj}^n = D_{kj} - D_{kn} = V_m \sum_{i=0}^n L_{ki}'' \frac{\partial^2 f}{\partial c_i \partial c_j} \quad (\text{B.17})$$

which can be written in the more compact matrix notation

$$D^n = V_m L'' \mathcal{T} \quad (\text{B.18})$$

with

$$\mathcal{T}_{ij} = \frac{\partial^2 f}{\partial c_i \partial c_j}. \quad (\text{B.19})$$

Appendix C. Non-linear system of equations to determine compositions in each phase

For a binary alloy composed of species A and B , we have free energy densities modeled in each phase Φ , liquid (L) and solid (S), by Eqs. (15)–(18).

The first derivative of f with respect to composition of A in phase Φ , c_Φ , is given by

$$\begin{aligned} V_m \frac{\partial f^\Phi}{\partial c_\Phi} &= RT [\ln c_\Phi - \ln(1 - c_\Phi)] \\ &+ (1 - 2c_\Phi) \\ &\quad [L_0^\Phi + L_1^\Phi (2c_\Phi - 1) + L_2^\Phi (2c_\Phi - 1)^2] \\ &+ c_\Phi (1 - c_\Phi) [2^1 L^\Phi + 4^2 L^\Phi (2c_\Phi - 1)] \\ &+ V_m [f_A^\Phi(T) - f_B^\Phi(T)]. \end{aligned} \quad (\text{C.1})$$

Let

$$\begin{aligned} \xi_\Phi &= (1 - 2c_\Phi) \\ &\quad [0 L^\Phi + 1 L^\Phi (2c_\Phi - 1) + 2 L^\Phi (2c_\Phi - 1)^2] \\ &+ c_\Phi (1 - c_\Phi) [2^1 L^\Phi + 4^2 L^\Phi (2c_\Phi - 1)] \\ &+ V_m [f_A^\Phi(T) - f_B^\Phi(T)], \end{aligned} \quad (\text{C.2})$$

so that (C.1) becomes

$$V_m \frac{\partial f^\Phi}{\partial c_\Phi} = RT \ln \frac{c_\Phi}{1 - c_\Phi} + \xi_\Phi. \quad (\text{C.3})$$

Using (7), we get

$$c_S(1 - c_L) = \exp \left(\frac{\xi_L - \xi_S}{RTV_m^{-1}} \right) (1 - c_S)c_L. \quad (\text{C.4})$$

Together with (6), we have a non-linear system of two equations. The two unknowns, c_L and c_S , can be solved by a suitable root-finding algorithm to enable calculation of the free energy densities f^L and f^S .

Appendix D. Au–Ni thermodynamic data

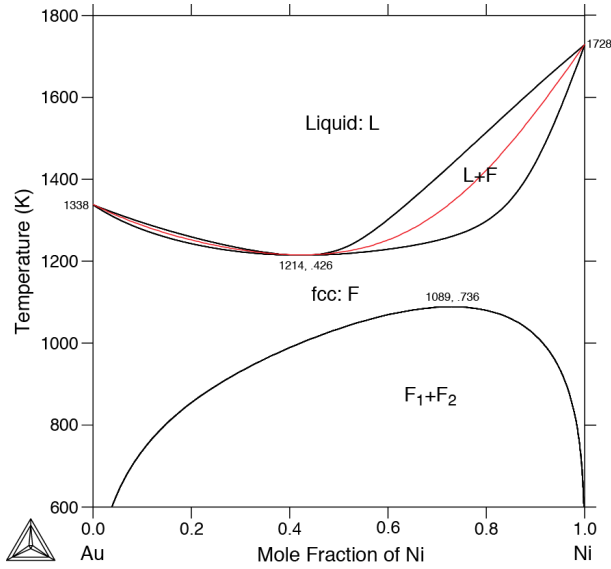


Figure D.15: Au–Ni phase diagram according to CALPHAD assessment of the thermodynamic properties.

The phase diagram of Au–Ni is shown in Fig. D.15. The CALPHAD description of the Gibbs energies for the liquid and solid (fcc) phases of Au–Ni are given in Tables D.2, D.3 and D.4, according to the assessment results discussed in [25]. Energies are expressed in J/mol and temperature T in Kelvin. The Gibbs energies of the pure elements are from [19] as given by the SSOL2 database of Thermo-Calc [22, 23].

$T[\text{K}]$	$298.15 \leq T \leq 933.51$	$\leq T \leq 1337.58$	$\leq T \leq 1735.8$	$\leq T \leq 3000$
Liquid				
a	5613.147	-81023.261	326614.987	413.343
b	97.446385	1012.21732	-2025.7579	155.893158
c	-22.75455	-155.6947	263.2523	-30.9616
d_2	-0.00385924	0.08756015	-0.11821685	0.
d_3	3.79625e-07	-1.1518713e-05	8.923845e-06	0.
d_{-1}	-25097.	10637210.	-67999850.	0.
Solid (fcc)				
a	-6938.853	-93575.261	314062.987	-12138.657
b	106.830495	1021.60143	-2016.37379	165.277268
c	-22.75455	-155.6947	263.2523	-30.9616
d_2	-0.00385924	0.08756015	-0.11821685	0.
d_3	3.79625e-07	-1.1518713e-05	8.923845e-06	0.
d_{-1}	-25097.	10637210.	-67999850.	0.

Table D.2: CALPHAD parametrization of the Gibbs energies of Au in liquid and solid (fcc) phases as functions of temperature T , with $H_{Au}^{SER}=6016.6$ and $S_{Au}^{SER}=47$, see Eq. (10). Units: J/mol.

Appendix E. Au–Ni kinetic data

The CALPHAD description of the mobilities for the liquid and fcc phases of Au–Ni are given according to the description discussed in section 3.6 and at the beginning of section 5.1. The parameters used to calculate the diffusion coefficients in Au–Ni in Eq. (33) are given in Table E.5. in the form $Q = \alpha + RT \ln(\beta)$ where α is given in Kelvin, and β is given in m^2/s with implicitly T in Kelvin and the gas constant $R=8.31451$ J/mol·K.

References

- [1] N. Moelans, B. Blanpain, P. Wollants, An introduction to phase-field modeling of microstructure evolution, CALPHAD 32 (2) (2008) 268–294.
- [2] U. Gfede, B. Böttger, J. Tiaden, S. G. Fries, Coupling of multicomponent thermodynamic databases to a phase field model: application to solidification and solid state transformations of superalloys, Scripta Materialia 42 (2000) 1179–1186.
- [3] J. Z. Zhu, Z. K. Liu, V. Vaithyanathan, L. Q. Chen, Linking phase-field model to CALPHAD: application to precipitate shape evolution in Ni-base alloys, Scr. Mater. 46 (2002) 401–406.
- [4] T. Pusztai, G. Bortel, L. Gránásy, Phase field theory of polycrystalline solidification in three dimensions, EPL (Europhysics Letters) 71 (1) (2005) 131–137.
- [5] M. R. Dorr, J. L. Fattebert, M. E. Wickett, J. F. Belak, P. E. A. Turchi, A numerical algorithm for the solution of a phase-field model of polycrystalline materials, J. Comput. Phys. 229 (2010) 626–641.
- [6] J.-O. Andersson, J. Agren, Models for numerical treatment of multicomponent diffusion in simple phases, J. Appl. Phys. 72 (4) (1992) 1350–1355.
- [7] J. Eiken, B. Böttger, I. Steinbach, Multiphase-field approach for multicomponent alloys with extrapolation scheme for numerical application, Phys. Rev. E 73 (6) (2006) 066122.
- [8] S. G. Kim, W. T. Kim, T. Suzuki, Phase-field model for binary alloys, Phys. Rev. E 60 (6) (1999) 7186–7197.
- [9] A. Borgenstam, A. Engström, L. Höglund, J. Agren, DICTRA, a tool for simulation of diffusional transformations in alloys, J. of Phase Equil. 21 (3) (2000) 269–280.
- [10] <http://www.thermocalc.com>.

$T[\text{K}]$	$298.15 \leq T \leq 1728$	$\leq T \leq 3000$
Liquid		
a	11235.527	-9549.775
b	108.457	268.598
c	-22.096	-43.1
d_2	-0.0048407	0.
d_7	-3.82318e-21	0.
Solid (fcc)		
a	-5179.159	-27840.655
b	117.854	279.135
c	-22.096	-43.1
d_2	-0.0048407	0.
d_{-9}	0.	1.12754e+31

Table D.3: CALPHAD parametrization of the Gibbs energies of Ni in liquid and solid (fcc) phases as functions of temperature T , with $H_{Ni}^{SER}=4787.0$ and $S_{Ni}^{SER}=29.796$, see Eq. (10). Units: J/mol.

Liquid		
${}^0L_{Au,Ni}^L$	=	9500. -5.429 T
${}^1L_{Au,Ni}^L$	=	1614.
Solid (fcc)		
${}^0L_{Au,Ni}^S$	=	28696. -11.274 T
${}^1L_{Au,Ni}^S$	=	-10945. + 6.154 T
${}^2L_{Au,Ni}^S$	=	2519.

Table D.4: CALPHAD values of the Redlich-Kister parameters that define the excess Gibbs energy according to Eq. (14) as functions of temperature T . Units: J/mol.

	Liquid		Solid	
	α	β	α	β
Q_{Au}^{Au}	-35921.87	3.1514e-08	-176600.	1.002878e-05
Q_{Ni}^{Ni}	-46353.23	5.9576e-08	-306500.	4.49132e-02
${}^0Q_{Au,Ni}^{Au}$	0.	1.	232300.	7.6881435e-08
${}^1Q_{Au,Ni}^{Au}$	0.	1.	15900.	1.
Q_{Ni}^{Au}	-35921.87	3.6471e-08	-188800.	1.702455873e-05
Q_{Ni}^{Ni}	-46353.23	6.8948e-08	-287000.	2.25994e-04
${}^0Q_{Au,Ni}^{Ni}$	0.	1.	136200.	1.
${}^1Q_{Au,Ni}^{Ni}$	0.	1.	-42800.	1.

Table E.5: Parametrization used in Redlich-Kister expansion of atomic mobilities coefficients in Au–Ni alloy, see Eq. (33).

- [11] F. N. Rhines, Phase diagrams in metallurgy - their development and applications, in: R. F. Mehl, M. B. Bever (Eds.), Metallurgy and Metallurgical Engineering series, McGraw-Hill Book Company, New York, 1956.
- [12] M. R. Harvey, J. L. Robbins, A. D. Wheeler, Homogenization of plutonium-1 wt% gallium alloys, *Micron* 5 (1975) 417–425.
- [13] N. Saunders, A. P. Miodownik, CALPHAD, calculation of phase diagrams: A comprehensive guide, in: Pergamon Materials Series, Vol. 1, Pergamon Press, Oxford, 1998.
- [14] A. P. Miodownik, Phenomenological calculations of phase equilibria: the CALPHAD approach, Vol. 319 of NATO-ASI Proceedings, Series B: Physics, Plenum Press, New York, 1994, pp. 45–79.
- [15] Computer simulations from thermodynamic data: Materials production and development, *MRS Bulletin* 24 (4) (1999) 18–49.
- [16] L. Kaufman, H. Bernstein, Computer Calculation of Phase Diagrams with Special Reference to Refractory Metals, Academic Press, New York, 1970.
- [17] P. E. A. Turchi, A. Gonis, R. D. Shull (Eds.), CALPHAD and Alloy Thermodynamics, TMS Publication, TMS, Warrendale, PA, 2002.
- [18] I. Ansara, B. Sundman, The Scientific Group ThermoData Europe, Computer Handling and Dissemination of Data.
- [19] A. Dinsdale, SGTE database for pure elements, *CALPHAD* 15 (1991) 317–425.
- [20] O. Redlich, A. Kister, Algebraic representation of the thermodynamic properties and the classification of solutions, *Ind. Eng. Chem.* 40 (1948) 345–348.
- [21] Y. M. Muggianu, M. Gambino, J. P. Bros, Enthalpies de formation des alliages liquides bismuth-étain-gallium à 723 K. Choix d’une représentation analytique des grandeurs d’excès intégrales et partielles de mélange, *J. Chem. Phys.* 22 (1975) 83–88.
- [22] B. Sundman, B. Jansson, J.-O. Andersson, The thermo-calc databank system, *CALPHAD* 9 (4) (1985) 153.
- [23] J.-O. Andersson, T. Helander, L. Höglund, P. Shi, B. Sundman, THERMO-CALC & DICTRA, computational tools for materials science, *CALPHAD* 26 (2) (2002) 273–312.
- [24] A. Engström, L. Höglund, J. Ågren, Computer simulations of diffusion in multiphase systems, *Metall. Mater. Trans. A* 25 (1994) 1127–1134.
- [25] J. Wang, X.-G. Lu, B. Sundman, X. Su, Thermodynamic assessment of the Au–Ni system, *CALPHAD* 29 (4) (2005) 263–268.
- [26] S. M. Allen, J. W. Cahn, A microscopic theory for antiphase boundary motion and its application to antiphase domain coarsening, *Acta Metallurgica*. 27 (1979) 1085–1095.
- [27] Y. Saad, M. H. Schulz, GMRES: A generalized minimal residual algorithm for solving nonsymmetric linear systems, *SIAM J. Sci. Stat. Comput.* 7 (1986) 856–869.
- [28] <https://computation.llnl.gov/casc/hypre/software.html>.
- [29] <https://simtk.org/home/cpodes>.
- [30] <https://computation.llnl.gov/casc/sundials/main.html>.
- [31] I. Steinbach, B. Böttger, J. Eiken, N. Warnken, S. G. Fries, CALPHAD and Phase-Field modeling: A successful liaison, *Journal of Phase Equilibria and Diffusion* 28 (1) (2007) 101–106.
- [32] J. Wang, L. B. Liu, H. S. Liu, Z. P. Jin, Assessment of the diffusional mobilities in the face-centred cubic Au–Ni alloys, *CALPHAD* 31 (2) (2007) 249 – 255.
- [33] Y. Liu, Z. Long, H. Wang, Y. Du, B. Huang, A predictive equation for solute diffusivity in liquid metals, *Scripta Mater.* (55) (2006) 367–370.
- [34] Q. Chen, N. Ma, K. Wu, Y. Wang, Quantitative phase field modeling of diffusion-controlled precipitate growth and dissolution in TiAlV, *Scripta Materiala* 50 (2004) 471–476.
- [35] S. Hu, M. Baskes, M. Stan, J. Mitchell, Phase-field modeling of coring structure evolution in PuGa alloys, *Acta Materialia* 55 (11) (2007) 3641–3648.
- [36] M. Plapp, Unified derivation of phase-field models for alloy solidification from a grand-potential functional, *Phys. Rev. E* 84 (3) (2011) 031601.
- [37] J. A. Warren, R. Kobayashi, A. E. Lobkovsky, W. C. Carter, Extending phase field models of solidification to polycrystalline materials, *Acta Materialia* 51 (20) (2003) 6035–6058.